Journal of Hazardous Materials 476 (2024) 135108

Contents lists available at ScienceDirect

Journal of Hazardous Materials

journal homepage: www.elsevier.com/locate/jhazmat

Phosphorus recovery via struvite crystallization in batch and fluidized-bed reactors: Roles of microplastics and dissolved organic matter

Junna Yan [a,1], Mengyu Ma [a,1], Feihu Li [a,b,*]

[a] Collaborative Innovation Center of Atmospheric Environment and Equipment Technology, Jiangsu Key Laboratory of Atmospheric Environment Monitoring and Pollution Control, School of Environmental Science and Engineering, Nanjing University of Information Science and Technology, 219 Ningliu Road, Nanjing 210044, China

[b] NUIST Reading Academy, Nanjing University of Information Science and Technology, 219 Ningliu Road, Nanjing 210044, China

HIGHLIGHTS

- Microplastics and humic acid act different roles in mediating struvite formation.
- Microplastics expedite the crystallization kinetic rate but humic acid reduces it.
- Microplastics serve as seeds facilitating struvite nucleation and growth.
- Humic acid favors the formation of newberyite but inhibits struvite formation.
- Both impurities affect the efficiency of P recovery and the quality of products.

GRAPHICAL ABSTRACT

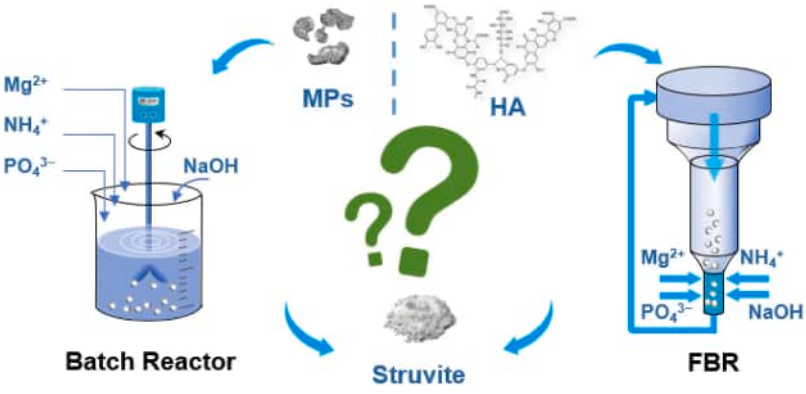

ARTICLE INFO

Keywords:
Struvite
Phosphorus recovery
Crystallization
Kinetics
Water purification

ABSTRACT

Struvite crystallization, a promising technology for nutrient recovery from wastewater, is facing considerable challenges due to the presence of emerging contaminants such as microplastics (MPs) ubiquitously found in wastewater. Here, we investigate the roles of MPs and humic acid (HA) in struvite crystallization in batch and fluidized-bed reactors (FBRs) using synthetic and real wastewater with a Mg:N:P molar ratio of 1:3:(1–1.3) at an initial pH of 11. Batch reactor (BR) experiment results show that MPs expedited the nucleation and growth rates of struvite (e.g., the rate of crystal growth in the presence of 30 mg L^{-1} of polyethylene terephthalate (PET) was 1.43 times higher than that in the blank system), while HA hindered the formation of struvite. X-ray diffraction and the Rietveld refinement analysis revealed that the presence of MPs and HA can result in significant changes in phase compositions of the reclaimed precipitates, with over 80 % purity of struvite found in the precipitates from suspensions in the presence of 30 mg L^{-1} of MPs. Further characterizations demonstrated that MPs act as seeds of struvite nucleation, spurring the formation of well-defined struvite, while HA favors the formation of

* Corresponding author at: Collaborative Innovation Center of Atmospheric Environment and Equipment Technology, Jiangsu Key Laboratory of Atmospheric Environment Monitoring and Pollution Control, School of Environmental Science and Engineering, Nanjing University of Information Science and Technology, 219 Ningliu Road, Nanjing 210044, China.
E-mail address: fhli@nuist.edu.cn (F. Li).
[1] These authors contributed equally to this work.

https://doi.org/10.1016/j.jhazmat.2024.135108
Received 27 April 2024; Received in revised form 2 July 2024; Accepted 4 July 2024
Available online 4 July 2024

newberyite rather than struvite in both reactors. These findings highlight the need for a more comprehensive understanding of the interactions between emerging contaminants and struvite crystallization processes to optimize nutrient recovery strategies for mitigating their adverse impact on the quality and yield of struvite-based fertilizers.

Environmental Implication: The presence of microplastics in wastewater poses a significant challenge to struvite crystallization for nutrient recovery, as it accelerates nucleation and growth rates of struvite crystals. This can lead to changes in the phase compositions of the reclaimed precipitates, with implications for the quality and yield of struvite-based fertilizers. Additionally, the presence of humic acid hinders the formation of struvite, favoring the formation of other minerals like newberyite. Understanding the interactions between emerging contaminants and struvite crystallization processes is crucial for optimizing nutrient recovery strategies and mitigating the environmental impact of these contaminants on water quality and struvite-based fertilizers.

1. Introduction

Phosphorus (P) is an essential element for the survival of all living organisms on our planet. Over 90 % of P in all the living beings on earth originated from ores, non-renewable resources [1,2]. The world population has been about 8.1 billion so far according to the most recent United Nations estimates, which will spur a growing demand for more mineral fertilizers for food production. This will no doubt accelerate the depletion of global phosphate rock reserves since more than 90 % of P ores were consumed in the production of fertilizers [3–5]. Moreover, quite much of P fertilizers are lost from the croplands or forestlands into waterways due to soil erosion [2] and find their way to the ocean eventually [6]. Such a one-way phosphorus flow (i.e., P flux from rock to ocean) is unsustainable considering the limitation in the supply of accessible phosphate rocks, and the impossibility of geologically replenishing these ores by natural phosphorus cycle [7]. It is therefore pressingly needed to develop efficient P recovery and recycling strategies for reclaiming this valuable element from P-rich streams and effluents (viz. secondary P resources), thus implementing a closed P cycle in the context of the circular economy.

Chemical precipitation has been demonstrated as one of the most promising approaches for P recovery from waste streams [8–11]. Over the past decades, struvite crystallization via chemical precipitation, in particular, has gained much more attention as the route strategy for P recovery and recycling due to its practical value to the fertilizer industry [1,12,13]. Historically, struvite formation and accumulation in municipal wastewater treatment plants (MWTPs) often cause operational issues, especially leading to the clogging of pipelines conveying supernatant from sludge digestion systems [14,15]. Nevertheless, a heap of benefits accompanied by P recovery through struvite crystallization have been identified, viz. the reduction in P and nitrogen load of side-stream and sludge liquors within pipelines of MWTPs, the decline of total sludge volumes, and more importantly the additional value for the MWTPs by commercializing the reclaimed struvite ($MgNH_4PO_4{\cdot}6H_2O$) as fertilizers [15–19]. Thereafter, extensive laboratory-scale investigations have been carried out worldwide [9,10,15,20–22], which have significantly advanced the practical application of this technology on an industrial scale [23,24].

Generally, both the struvite crystallization process and the quality of reclaimed struvite are usually determined by the water compositional chemistry of the synthetic solutions [15,25]. Specifically, solution pH, the molar ratio of Mg:N:P, and the presence of foreign species (i.e., impurities) collectively play a critical role in regulating the crystallization process [12,26–28]. Solution pH is one of the major factors affecting the crystallization process and the final quality of struvite formed [12,15]. An optimal pH range of 8.5 − 9.5 was identified for the precipitation rate of struvite for a synthetic solution with Mg:N:P molar ratio of 1:1:1 [29]. Besides, pH ranging from 8 − 11 was also employed for solutions beyond this molar ratio [30,31], because real waste streams often contain a large molar excess of ammonium ions (NH_4^+) [11], and a higher pH can lead to the transformation of NH_4^+ to gaseous ammonia (NH_3), hence influencing the Mg:N:P molar ratio [12].

The presence of impurities, such as inorganic ions, and dissolved organic matter (DOM) can significantly impact the nucleation and crystal growth of struvite. For instance, sulfate (SO_4^{2-}) has been found to affect the precipitation of struvite by prolonging the induction time, since the free SO_4^{2-} is likely to be complexed with NH_4^+ and Mg^{2+} [26]. Likewise, DOMs such as humic acid (HA) [32,33], alginic acid [34], phenolic organics [35], citrate and phosphocitrate [36] can be complexed with the struvite component ions (e.g., NH_4^+ and Mg^{2+}) or attach to the crystal nuclei, thus demonstrating an inhibitory impact on struvite precipitation. For example, it was well documented that the presence of HA even at a low concentration (e.g., 10 mg L^{-1}) appears to hinder struvite formation by covering the crystal nuclei [32]. Furthermore, changes in solution pH can alter the speciation of these compounds, thereby affecting their impact on struvite formation. Apart from the crystallization process, and more importantly, the cooccurring of toxic impurities such as heavy metals, antibiotics, and antibiotic resistance genes (ARGs), can pose a biosecurity issue to the croplands where the reclaimed struvite was applied [33,37–40].

Moreover, recent studies indicated that microplastics (MPs) are omnipresent in environmental media, including nutrient-rich waste streams [41,42]. MPs can act as a vector of toxins [43] and are likely to be encapsulated in calcium carbonate sediments when exposed to DOMs [44]. However, little is known about the effects of MPs along with HA on the struvite formation kinetic as well as the quality of struvite crystals, especially in the context of P recovery from nutrient-rich waste streams via struvite crystallization. It is also not known whether MPs can act as a deposition platform or nucleation seeds for struvite.

To this end, this study aims to identify how aged MPs and DOM molecules influence the crystallization kinetics and the quality of struvite in BRs and FBRs (Scheme 1) under ambient conditions. HA was selected as the model DOM molecule, while aged polyethylene (PE) and polyethylene terephthalate (PET) particulates were chosen to represent MPs. Trace heavy metals (HMs) such as Cu^{2+} and Zn^{2+} ions are likely to be found in nutrient-rich streams (e.g., swine wastewater) and bound to the surface of MPs [45,46]. Two aged MP suspensions were dispersed and loaded with dissolved Cu^{2+} or Zn^{2+} individually before applying in the struvite crystallization experiments. The suspension pH and the dissolved phosphate concentration were monitored to study the crystallization kinetics. X-ray diffraction (XRD), X-ray fluorescence (XRF) analysis, and Fourier-transform infrared (FTIR) spectroscopy were used to investigate the quality of reclaimed struvite. This work brings a crucial insight into a previously underexplored interaction between MPs, humic substances, and crystal-forming ions during the phosphorus recovery process, shedding light on how these impurities influence the crystallization of struvite in BRs and FBRs.

2. Materials and methods

2.1. Materials

All chemicals used for struvite crystallization are of analytical pure grade. Monopotassium phosphate (KH_2PO_4, ≥99.0 %), magnesium

chloride ($MgCl_2$, ≥98.0 %), sodium hydroxide (NaOH, ≥99.0 %), and ammonium magnesium phosphate hexahydrate ($MgNH_4PO_4{\cdot}6H_2O$, 98.0 %) were purchased from Sinopharm Chemical Reagent Co., Ltd. (Shanghai, China). Ammonium chloride (NH_4Cl, 99.5 %) was obtained from Macklin Biochemical Co., Ltd. (Shanghai, China). Humic acid (HA) was provided by Shanghai Yuanye Bio-Technology Co., Ltd (Shanghai, China). The microplastics (MPs), polyethylene (PE), and polyethylene terephthalate (PET) of ca. 50 μm in size were purchased from Wangda Plastic Material Co., Ltd. (Dongguan, China) and artificially aged over 20 days using a heat persulfate oxidation method. After loading with copper or zinc ions in a set of adsorption experiments [46], the metal-loaded MPs (denoted by PE-Cu, PE-Zn, PET-Cu, and PET-Zn, respectively) were used as impurities in the struvite crystallization experiments. Considering that both PE and PET are likely to bind HMs rapidly in natural and wastewater systems [45,46], and that many previous studies have already explored the effect of sole or mixed HMs on struvite precipitation [47–49], the choice of metal-loaded MPs as impurities is deliberate and more environmentally relevant because the MP-HM complex rather than the MPs or HMs individual predominate in either the simulated or the real piggery/swine effluents. Ultrapure deionized (DI) water (18.2 MΩ·cm, 25 °C) was employed for preparing solutions.

2.2. Struvite crystallization in a batch reactor (BR)

The batch crystallization kinetic experiments were carried out with a constant Mg:N:P molar ratio of 1:3:1 in a 1000-mL beaker (Fig. S1a, Supporting Information) at standard atmospheric pressure and temperature (ca. 25 °C). In brief, solution A was prepared by dissolving 0.83 mmol of KH_2PO_4 into 493 mL of DI water, to which a dilute NaOH solution was added to adjust the pH to 11 ± 0.2. Likewise, solution B was synthesized by combining 0.83 mmol of $MgCl_2$ and 2.5 mmol of NH_4Cl with 7 mL of DI water, which was then quickly poured into the beaker with solution A and mixed moderately over a magnetic stirrer (INTLLAB, Shenzhen, China). The pH of the synthetic mixture was monitored using a pH meter (PHS-25, Rex Electric Chemical) and recorded every minute for 60 min, while the concentration of remaining soluble phosphate (PO_4^{3-}-P) was measured every 5 min following the ascorbic acid method as described elsewhere [50]. Five mL of suspension was sampled at 5-minute intervals and immediately forced through a 0.45-μm mixed cellulose ester membrane filter mounted with a syringe. The filtrate was then acidized with 20 μL of 6 M HCl to stop the crystallization reaction [51]. Next, the concentration of soluble phosphate was determined using a JH723PC visible spectrophotometer (Shanghai, China). The effects of aged MPs and HA on the crystallization kinetics were studied following the same protocols with the addition of a certain amount of such specific impurities. Specifically, the aged MP impurities were added to the mixture individually at the beginning of the mixing of solutions A and B. Based on limited data available on microplastic abundances in swine wastewater [52,53], two MP levels (i.e., 3 and 30 mg L^{-1}) were chosen to simulate the cases at environmentally relevant and worst-case concentrations, respectively. The resulting suspension was denoted by the impurity in the mixture, e.g., PET-Cu-3 refers to suspension in the presence of 3 mg L^{-1} of PET-Cu as the impurities.

All the precipitate samples were collected centrifugally after the termination of each batch reaction (i.e., 60 min), followed by rinsing twice with DI water and drying in an oven at 80 °C overnight. After cooling down to ambient temperature in a glass desiccator, the precipitates were labeled with the same sample code as the parent suspensions and stored in the desiccator for further characterization. The crystallization kinetic rate constant was determined by fitting the data of remaining soluble phosphate in the suspensions to a first-order kinetic model that is expressed in differential and linear forms as formulated in Eq.1 and Eq.2, respectively [51].

$$-\frac{dC}{dt} = k(C_0 - C_e) \tag{1}$$

$$\ln(C - C_e) = -kt + \ln(C_0 - C_e) \tag{2}$$

Where $\boldsymbol{k}$ is the rate constant (h^{-1}), $\boldsymbol{C}$ is the soluble phosphate (reactant) concentration (mg L^{-1}) at time $\boldsymbol{t}$, $\boldsymbol{C}_0$ and $\boldsymbol{C}_e$ are the phosphate (PO_4^{3-}-P) concentration at initial and equilibrium state (mmol L^{-1}).

2.3. Struvite crystallization in an FBR

Struvite formation kinetic experiments were also performed in a customer-made FBR (Fig. S1b, Supporting Information) [31]. The phosphate-enriched effluents were from a set of rapid adsorption-desorption enrichment operations as described in our earlier works [54,55]. The FBR feed solution (~ 5 L) was prepared by combining the phosphate-enriched effluents with certain amounts of $MgCl_2$ and NH_4Cl to achieve a final Mg:N:P molar ratio of 1.3:4:1 [26]. Sodium hydroxide (NaOH) solution (0.1 M) was used as the alkaline solution to adjust the initial pH of the feed solution to above 11 within

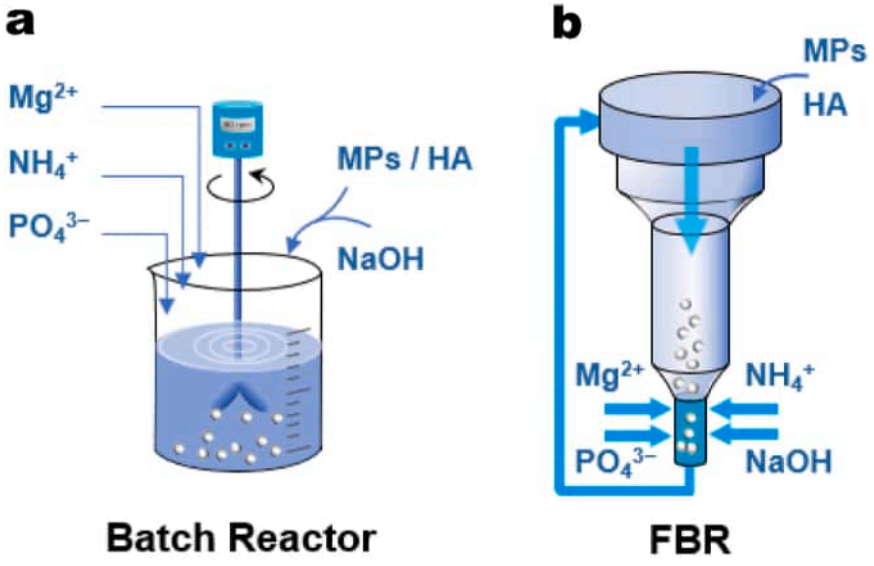

Scheme 1. (**a**) Batch reactor (BR), and (**b**) fluidized-bed reactor (FBR) for struvite crystallization.

the FBR setup. To start with, the feed solution was fed into the FBR at a flow rate of 5 mL min^{-1} for 5 min using a peristaltic pump (BT-100, Longer Pump Co., China). Next, the NaOH solution was fed at a flow rate of 3 mL min^{-1} using another pump, while the third pump linking the bottom and the upper top of the FBR setup was launched meanwhile at 10 mL min^{-1} to circulate the mixture and keep a fluidization state.

After circulating for 6 days, the experiment was terminated and the struvite precipitates were reclaimed from the FBR bottom (Fig. S1b), followed by centrifugal separating, rinsing thrice with DI water, and air drying over 24 h before further characterization. The effects of seed ($MgNH_4PO_4{\cdot}6H_2O$, 98.0 %), and PET impurity on struvite formation in FBRs were investigated with individual addition of different amounts of such impurity at the beginning of each circulating operation. Actual wastewater (WW) from a local sewage treatment plant (Table S1) was used to explore the effect of natural DOM on struvite formation.

2.4. Characterization of the reclaimed precipitates

X-ray diffraction (XRD) analysis was conducted on a Shimadzu XRD-6100 diffractometer with Cu-K radiation (λ = 1.54178 Å) over the 2θ range of 10 – 60°. All the mineral phases were identified using the Jade software (version 6.5, Materials Data, Inc., USA) with the ICDD® PDF-2 database. Mass percentages of mineral phase in the reclaimed precipitates were calculated by the whole-pattern fitting (WPF) module embedded in Jade software. Using the soil mode, the elemental composites of the reclaimed precipitates were recorded using a handheld X-ray fluorescence (XRF) spectrometer of the DELTA series DC-4000 (Olympus, USA). A Nicolet iS5 spectrometer (Thermo Fisher, USA) was used for Fourier transform infrared (FTIR) spectroscopy acquisition over the wavelength range of 4000 – 400 cm^{-1} using the KBr pellet method. Scanning electron microscopy (SEM) was performed using an SU1510 electron microscope (Hitachi, Japan) at an accelerating voltage of 15 kV.

3. Results and Discussions

3.1. Effect of MPs on the kinetics of struvite formation in BRs

Apart from Mg^{2+}, there are no other species (e.g., Ca^{2+} or DOM) in the suspensions that can form precipitates or complexes with phosphate, so the likelihood of struvite formation can be verified by monitoring the decrease in PO_4^{3-}-P concentration and the pH, thereby determining the kinetics of struvite crystallization indirectly. Note that there are other phosphate phases (e.g., newberyite) in the precipitate in addition to struvite, it is not strictly accurate to refer to the precipitate by struvite alone. However, considering that the stoichiometric coefficients in both newberyite and struvite are 1, for the sake of simplicity, struvite is used to refer to the precipitates in the kinetics sections.

As shown in Fig. 1a-b, both the pH and the soluble PO_4^{3-}-P in the suspension denoted blank decreased rapidly with reaction time, declining linearly with time at initial 10 min and then approaching to equilibrium state at about 40, and 20 min, respectively. Generally, struvite formation in a homogenous solution often takes place in two stages: nucleation and growth [12,56]. The struvite formation reaction

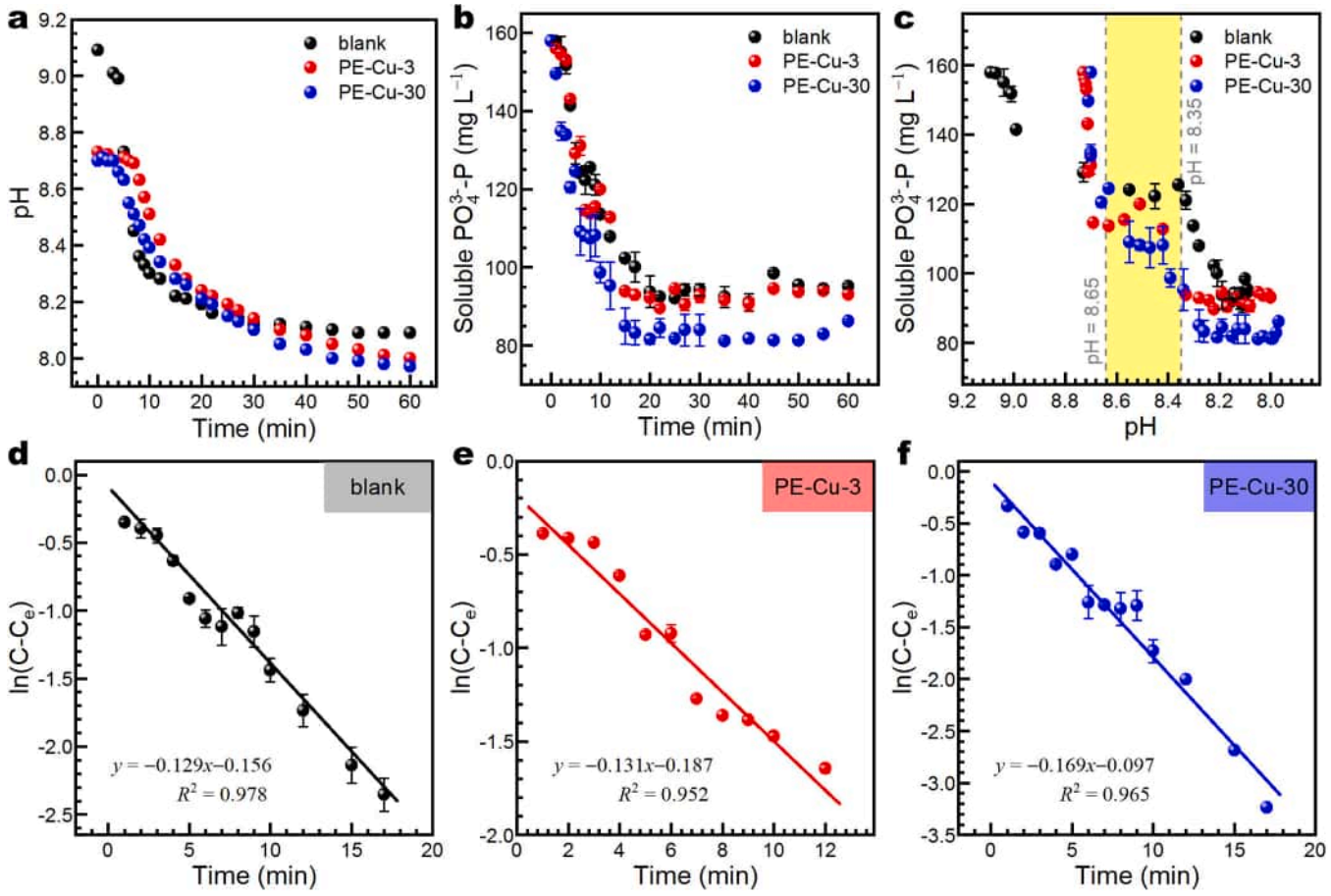

Fig. 1. (**a**) The suspension pH profiles, (**b**) Plots of soluble PO_4^{3-}-P versus reaction time Plots of soluble PO_4^{3-}-P versus pH, (**c**) Plots of soluble PO_4^{3-}-P versus pH during the struvite crystallization in batch reactors with varying contents of PE-Cu (Note: blank, PE-Cu-3 and PE-Cu-30 stand for 0, 3, and 30 ppm, respectively; the yellow shaded region in panel **c** represents a lag phase of struvite formation at pH 8.35 – 8.65 possibly due to nucleation kinetics); (**d-f**) Kinetic linear fitting plots of soluble phosphate concentration versus time in suspensions with (**d**) 0, (**e**) 3, and (**f**) 30 ppm of PE-Cu.

would consume a large amount of PO_4^{3-}, which shifts the equilibrium of orthophosphate species to the right-hand side (i.e., $H_3PO_4 \leftrightarrow H_2PO_4^- + H^+ \leftrightarrow HPO_4^{2-} + 2H^+ \leftrightarrow PO_4^{3-} + 3H^+$), releasing a lot of protons to the suspension and thereby lowering its pH eventually. Hence, pH was usually used as an indicator to monitor the nucleation process [57]. It was found that the initial nucleation rate of struvite is extremely fast when the suspension pH is > 9 [51], which is consistent with the observed rapid decrease in pH and soluble-PO_4^{3-}-P concentration (Fig. 1a-b).

Note that a distinct lag phase developed as the suspension pH fell from above 9 to the range of 8.65 − 8.35 (the yellow-shaded region in Fig. 1c), which is likely attributed to the reduced nucleation kinetics by the decrease in pH [51]. Note that in Fig. 1c, the pH range beyond 8.35 – 8.2 (corresponding to reaction time 10–30 min in Fig. 1a) appears to be attributed to the growth stage accordingly. In addition to changes in pH and soluble PO_4^{3-}-P concentration, the declines in soluble Mg^{2+} and NH_4^+ also indicated the two-stage formation pattern of struvite (Fig. S2a-b). Moreover, an attempt to monitor the pH changes in synthetic solutions with varying Mg^{2+} concentrations also demonstrated this growth pattern (Fig. S2c). With an assumption that the inverse reaction of struvite formation is minimal and negligible, the data recorded in the initial metastable stage before achieving an equilibrium state (0–16 min) was chosen to fit with the first-order kinetic model (Eq. 2), and the best-fit kinetic equations and corresponding parameters are tabulated in Table 1. The fit coefficient (R^2) is as high as 0.978 for the suspension blank, indicating the first-order kinetic model is reasonable enough to describe and predict the changes in soluble PO_4^{3-}-P concentration (Fig. 1d). The rate constant of 7.74 h^{-1} is less than that reported earlier at pH 9 (i.e., 12.3 h^{-1}) [51], which is likely due to the difference of the struvite-forming ion concentration and ratios applied that defines the supersaturation of the resulting solutions. Supersaturation is believed to be the primary influence on the struvite formation induction time provided that mixing is sufficient [57]. Moreover, the induction time has been included in our case while it seems to be excluded by Nelson *et al.* [51], as evidenced by the difference in the time range selected (0 −16 min versus 2 −9 min). This also contributed to the relatively less kinetic rate constant in the current study.

When the aged MP impurities were introduced into the suspensions, for instance, PE-Cu particulates (i.e., PE-Cu-3, and PE-Cu-30), the initial pH dropped from 9.1 to ~ 8.7 (Fig. 1a), possibly since all the MP particulates were aged by the heat persulfate oxidation (HPO) and preloaded copper or zinc ions in suspension at pH 6 [46]. Similar plots of PO_4^{3-}-P versus time in the presence of PE-Cu as that of blank demonstrates that struvite was formed in a similar way (Fig. 1b). The observed changes in Mg^{2+} and NH_4^+ also verified this speculation (Fig. S2a-b). More importantly, note that the more the PE-Cu impurities are introduced, the faster the soluble PO_4^{3-}-P concentration reaches a steady state in the initial 20 min (Fig. 1b), suggesting that the introduction of PE-Cu can facilitate the struvite formation. Likewise, the lag phases appeared once again in the plots of PO_4^{3-}-P versus pH in suspension with PE-Cu impurities as pH fell within the range of 8.65–8.35 (Fig. 1c), but the pH span is narrower than that of the blank sample, indicating that the presence of PE-Cu also enhances the nucleation kinetics. In addition, the linearities of both experimental data with PE-Cu impurities show a good fit ($R^2 > 0.95$, Fig. 1e-f), demonstrating that the first-order kinetic model is reasonable in predicting the decrease in the logarithmic concentration of soluble PO_4^{3-}-P in suspensions with PE-Cu impurities. The kinetic rate constants are 7.86, and 10.14 h^{-1} for PE-Cu-3, and PE-Cu-30, respectively (Table 1), both greater than that for the blank suspension, confirming the positive effect of PE-Cu in promoting struvite formation in BRs.

Similarly, the same trends of pH and soluble PO_4^{3-}-P concentration with time have also been observed in the cases of suspensions with other impurities including PET-Cu (Fig. 2a-b), PE-Zn (Fig. S3a-b), and PET-Zn (Fig. S4a-b). The kinetic fitting results (Table 1) demonstrated high linearity (Fig. 2c-d, Fig. S3c-d, Fig. S4c-d) as well, confirming the generalized applicability of the first-order model in describing the change of soluble PO_4^{3-}-P in these suspensions with varying impurities during the struvite formation process. For instance, the presence of 30 ppm of PET-Zn demonstrated the most rapid crystallization kinetic rate, 1.43 times the blank (Table 1). Recall that the introduction of these MP impurities can somewhat decrease the initial pH (Figs. 1b, 2b), thereby increase the induction time by depressing the nucleation kinetics [51,58]. This speculation is evidenced by the slightly lower rate constants of suspensions with 3 mg L^{-1} of MP impurities than that of the blank suspension (Table 1). However, the addition of more MP impurities into these suspensions (i.e., up to 30 mg L^{-1}) can distinctly offset the reduced nucleation kinetics caused by the decline in pH, as revealed by the higher rate constants compared to that of the blank suspension (i.e., $k_{PE\text{-}Zn\text{-}30} > k_{PE\text{-}Cu\text{-}30} > k_{PET\text{-}Cu\text{-}30} > k_{PET\text{-}Zn\text{-}30} > k_{blank}$, see Table 1).

3.2. Effect of HA and MPs on the kinetics of struvite formation in BRs

Recall that HA is believed to inhibit the crystallization of struvite [32,33]. As shown in Fig. 3a-b, the decreases in both the suspension pH and the soluble PO_4^{3-}-P concentration with time are slower in the presence of HA relative to those of blank, indicating the inhibitory impact of HA on the formation of struvite. Using *in situ* liquid-cell atomic force microscopy, Ge et al. observed that HA can greatly stabilize amorphous calcium phosphate by the formation of molecular organo-mineral bonding, thereby delaying the crystallization of thermodynamically stable calcium phosphate [59]. It was found that HA preferentially binds divalent or trivalent cations by forming humic-metal complexes of medium to high stability, which is likely to further bind P and form humic-metal-P complexes in aqueous solutions [60]. Interestingly, the initial pH of these suspensions with HA has been

Table 1
Best-fit kinetic equations and corresponding parameters of struvite crystallization in batch reactors with varying contents of impurities derived from the first-order model (Eq. 2).

Suspension code	Impurity	Content (ppm)	First-order kinetic equation	k (h^{-1})	Time Range	R^2
blank	none	0	$y = -0.129x - 0.156$	7.74 ± 0.44	0 – 16 min	0.978
PE-Cu-3	PE-Cu	3	$y = -0.131x - 0.187$	7.86 ± 0.59	0 – 12 min	0.952
PE-Cu-30	PE-Cu	30	$y = -0.169x - 0.097$	10.14 ± 0.58	0 – 16 min	0.965
PET-Cu-3	PET-Cu	3	$y = -0.117x - 0.334$	7.02 ± 0.62	0 – 12 min	0.941
PET-Cu-30	PET-Cu	30	$y = -0.136x - 0.076$	8.16 ± 0.72	0 – 12 min	0.935
PE-Zn-3	PE-Zn	3	$y = -0.120x - 0.279$	7.20 ± 0.61	0 – 12 min	0.939
PE-Zn-30	PE-Zn	30	$y = -0.184x - 0.136$	11.04 ± 1.16	0 – 12 min	0.919
PET-Zn-3	PET-Zn	3	$y = -0.118x - 0.337$	7.08 ± 0.51	0 – 10 min	0.960
PET-Zn-30	PET-Zn	30	$y = -0.133x - 0.187$	7.98 ± 0.43	0 – 10 min	0.977
HA-10	HA	10	$y = -0.336x - 0.410$	20.16 ± 2.97[a]	0 – 4 min	0.958
HA-100	HA	100	$y = -0.457x - 0.739$	27.42 ± 0.60[a]	0 – 4 min	0.999
HA+PET-Cu	HA, PET-Cu	10, 30	$y = -0.096x - 0.501$	5.76 ± 0.62	0 – 10 min	0.916

[a] hese high k values would not contribute to the struvite formation reaction but to the complexation reactions between HA, metal ions, and phosphate [59,60].

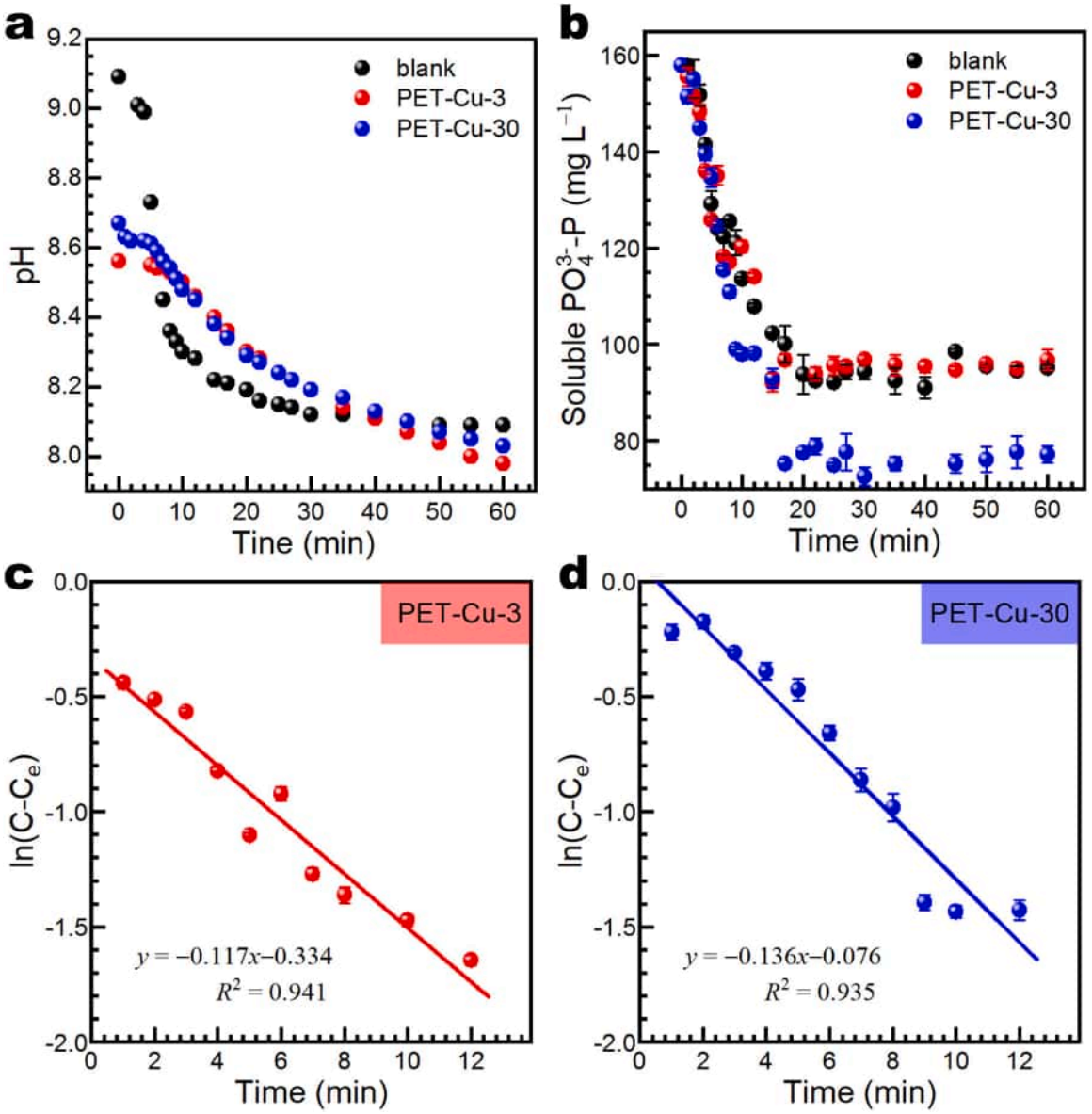

Fig. 2. (**a**) The suspension pH profiles, (**b**) Plots of soluble PO_4^{3-}-P versus reaction time in suspensions with varying contents of PET-Cu; (**c**) Kinetic linear fitting plots of soluble PO_4^{3-}-P in suspensions with (**c**) 3 ppm and (**d**) 30 ppm of PET-Cu.

increased by 0.2 and 0.5 units for the suspension HA-10 and HA-100, respectively, possibly due to the higher affinity of HA toward protons [61]. Preceding reports suspected that organic acids are likely to complex with Mg^{2+} and NH_4^+ to form complexes of high thermodynamical stability and release protons meanwhile, leading to the gradual decrease in solution supersaturation and the significant increase in free energy barrier for nucleation and thus the induction time [32,62]. Besides, these organic acids may be sorbed over the active sites of the nuclei, yielding molecular organo-mineral complexes of high stability and thus blocking the struvite crystal growth [32,59].

Note that the linear fitting and description of the logarithmic concentration of soluble PO_4^{3-}-P versus time using the first-order model (Eq. 2) failed in suspensions of HA over the range of 0 − 10 min (Fig. 3c-d). However, the logarithmic concentration of soluble PO_4^{3-}-P showed excellent linearity against time in the range of 0–4 min, with rate constants (k) as high as 20.16, and 27.42 h^{-1} for suspension HA-10, and HA-100, respectively (Table 1). Such higher k values would not be attributed to the struvite formation reaction based on the above explanation, but probably to the formation of HA-metal-phosphate complexes of high thermodynamical stability [59,60]. Interestingly, when co-introducing 10 mg $L^{-1}$of HA and 30 mg $L^{-1}$of PET-Cu into the blank suspension (i.e., the HA+PET-Cu suspension), the plot of pH versus time changed slightly whereas the plot of soluble PO_4^{3-}-P versus time varied remarkably (Fig. 3a-b). This observation indicates that the pH values are primarily governed by the HA, while the induction time is dominated by PET-Cu. Note that the first-order model demonstrates a good fit in describing the logarithmic concentration of soluble PO_4^{3-}-P against time in suspension HA+PET-Cu (Fig. 3e), with a rate constant of 5.76 h^{-1} (Table 1). In comparison with suspensions blank and PET-Cu-30, the rate constants follow the order $k_{\text{PET-Cu-30}} > k_{\text{blank}} > k_{\text{HA+PET-Cu}}$, indicating that PET-Cu and HA played exactly opposite roles in struvite formation. Collectively, HA molecules appear to inhibit struvite formation by a set of complexation reactions even at a low content (e.g., 10 mg L^{-1}), and MPs are likely to compensate for this inhibitory influence of HA by reducing the induction time and thereof facilitate the crystallization of struvite in the complex suspensions.

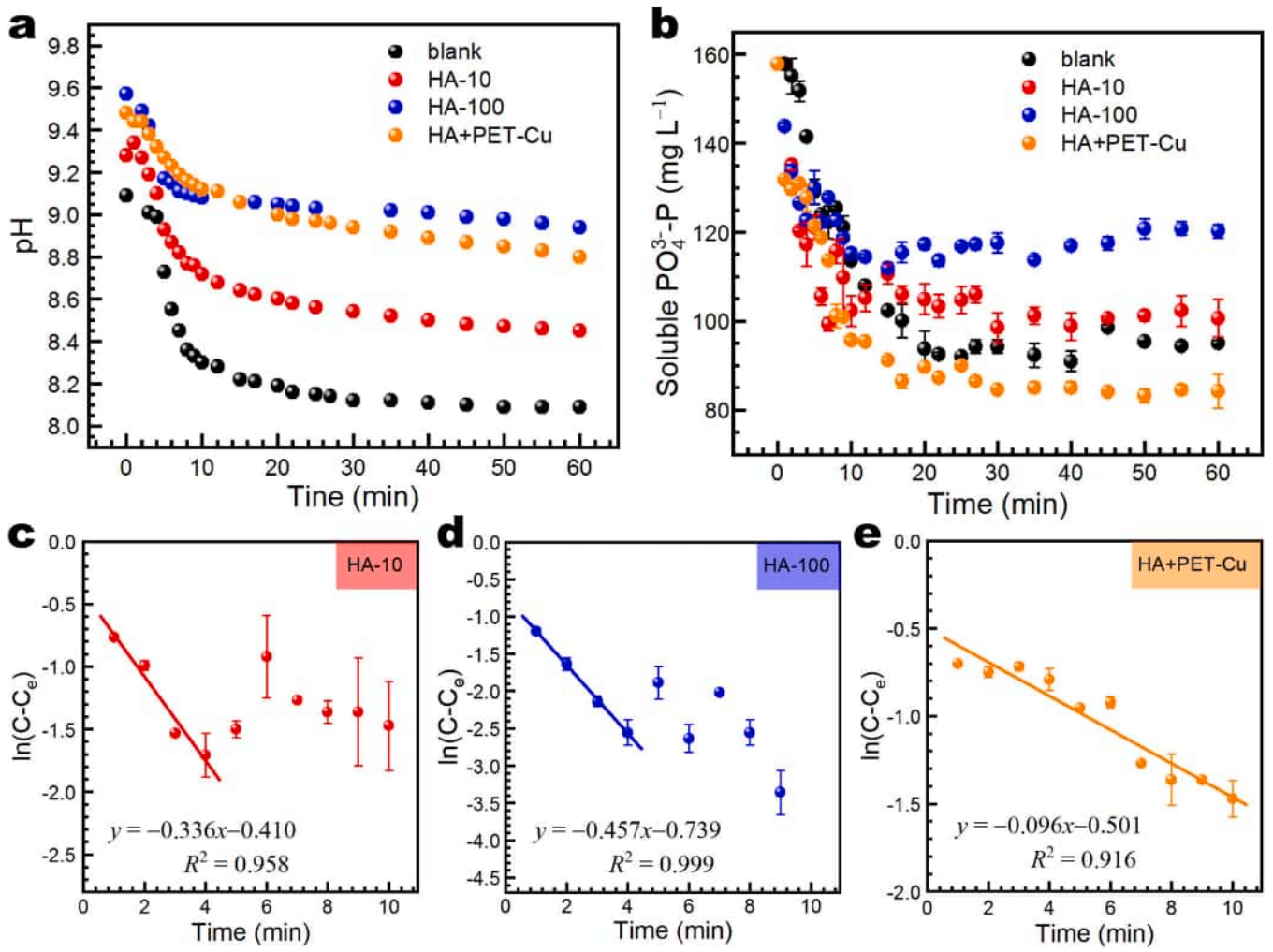

Fig. 3. (**a**) The suspension pH profiles, (**b**) Plots of soluble PO_4^{3-}-P versus reaction time in suspensions with varying contents of HA and PET-Cu; (**c**) Kinetic linear fitting plots of soluble PO_4^{3-}-P in suspensions with (**c**) 10 ppm of HA, (**d**) 100 ppm of HA, and (**e**) 10 ppm of HA + 30 ppm of PET-Cu (denoted by HA+PET-Cu).

3.3. Effect of MPs on the precipitates reclaimed from BRs

Apart from the influence on the kinetic of struvite formation, both MPs and HA also played different roles in regulating the physiochemical properties (e.g., morphologies, chemical, and phase compositions) of the resulting precipitates in BRs. In the absence of any impurities (i.e., the blank suspension), for instance, the precipitate (denoted as blank) demonstrated a well-defined XRD pattern (Fig. 4a). By using the Rietveld refinement algorithm (i.e., the WPF refinement module in Jade version 6.5), we calculated that the phase compositions of the precipitate blank are 16.6 wt% newberyite ($MgHPO_4{\cdot}3H_2O$, JCPDS #75–1714), 32 wt% halite (NaCl, JCPDS #70–2509), and 51.4 wt% sal-ammoniac (NH_4Cl, JCPDS #73–0365) (Fig. 4b). XRF and FTIR spectra revealed that its major chemical compositions (P, K, Cl, *etc.*, Figs. S5c) and functional groups ($\nu_{P\text{-}O}$, $\nu_{N\text{-}H}$, and $\nu_{O\text{-}H}$, Fig. 4c), are highly identical to the XRD results (Fig. 4a-b). Moreover, the SEM images showed that the blank precipitate is composed of well-defined microcrystal mixtures (Fig. 4d_1), with cubic halite (marked by a yellow arrow, Fig. 4d_2), newberyite microrods (marked by a blue arrow, Fig. 4d_2), and irregular-shaped sal-ammoniac.

Interestingly, there were clear changes in the XRD pattern of the reclaimed precipitate when 3 mg L^{-1} (ppm) of PE-Cu was introduced (red line labeled as PE-Cu-3, Fig. 4a), with increasing intensities of newberyite and disappearing of other phases. Similar changes were also observed in the XRD pattern of precipitate reclaimed from BRs with 3 ppm of PE-Zn (red line, Fig. S5a). The WPF refinement results indicated that there are 96.7 wt% of newberyite, 2.9 wt% of $MgHPO_4{\cdot}xH_2O$ (JCPDS #46–0375), and trace magnesite ($MgCO_3$, JCPDS #80–0101) in precipitate PE-Cu-3 (Fig. 4b), while PE-Zn-3 is composed of 95.8 wt% newberyite and 4.2 wt% struvite (JCPDS #71–2089, Fig. S5b). These observations suggest that the presence of PE impurities, irrespective of the metal ions loaded, can facilitate the formation of newberyite. This is evidenced by the corresponding FTIR spectra with greater intensities of $\nu_{P\text{-}O}$ vibrations (e.g., P-O stretching at 1004 cm^{-1}) and less intensities of $\nu_{N\text{-}H}$ vibration at 1427 cm^{-1} compared to those observed in the blank precipitate (Fig. 4c, S5d). Besides, SEM images show that rod-like newberyite embedded in PE surface dominates in precipitate PE-Cu-3 (Fig. 4e), whereas PE-Zn-3 is predominant by irregular scale-like newberyite grew over the surface of PE particulates (Fig. S6b). Therefore, it's reasonable to speculate that PE particulates (highlighted with PE in Fig. 4) govern the phase transformation while the metal ions loaded on PE (viz. Cu^{2+}, Zn^{2+}) regulate the morphology of the resulting newberyite. It is worth noting that both precipitates were dominated by struvite when 30 ppm of PE-Cu or PE-Zn were added into the BRs, with 92.3 wt% and 80 wt% struvite in PE-Cu-30 and PE-Zn-30, respectively (Fig. 4a-b, S5a-b). Molecular spectrum results (Fig. 4c, S5c-d) also demonstrate the above observations. Note that the surfaces of PE particulates were embedded by many irregular struvite microcrystals (Fig. 4f, S6c), implying PE impurities, in particular the cracked or defective domains, can serve as centers for nucleation and

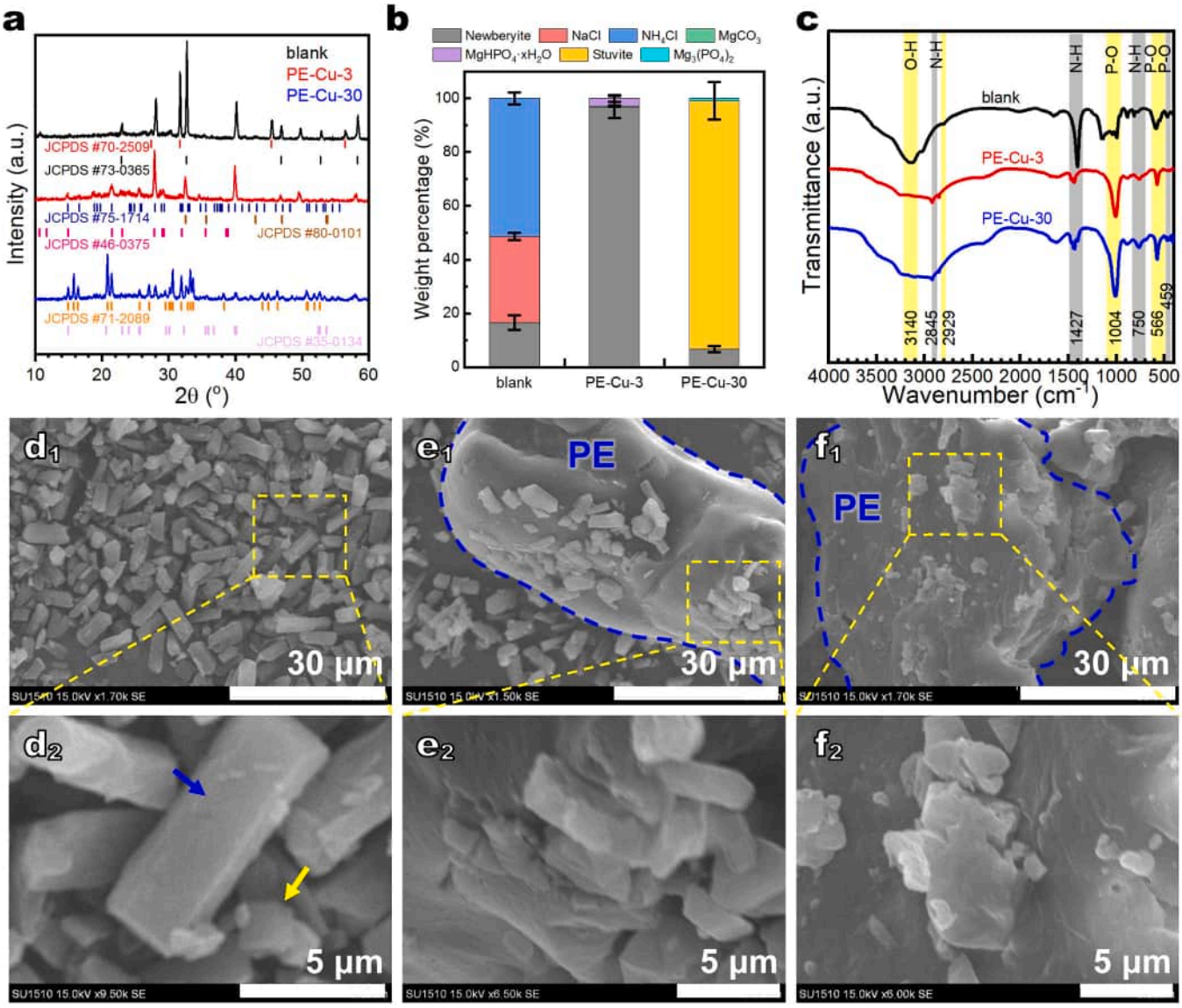

Fig. 4. Characterizations of precipitates from batch reactors in the absence or presence of PE-Cu impurities. (**a**) XRD patterns (newberyite, JCPDS #75–1714; halite, JCPDS #70–2509; sal-ammoniac, JCPDS #73–0365; $MgHPO_4{\cdot}xH_2O$, JCPDS #46–0375; magnesite, JCPDS #80–0101; struvite, JCPDS #71–2089; $Mg_3(PO_4)_2$, JCPDS #35–0134), (**b**) phase compositions, (**c**) FTIR spectra; SEM images of (**d**) the control sample (i.e., precipitate from the blank suspension), (**e**) the reclaimed samples with 3 mg L^{-1} PE-Cu, and (**f**) 30 mg L^{-1} PE-Cu.

crystallization of struvite and newberyite [12,58]. Given the fact that the presence of 3 ppm PE-Cu or PE-Zn favored the formation of newberyite while the addition of 30 ppm of PE facilitated the transformation from newberyite to struvite (Fig. 4b, S5b), we can conclude that newberyite is less thermodynamically stable in the pH region studied but struvite is more sensitive to co-occurring impurities [63].

Notably, no newberyite was found in the precipitates in the presence of PET impurities, regardless of the metals loaded and their contents in the reaction suspensions (Fig. 5, S7). Only rod-like struvite and amorphous components were identified in these precipitates (i.e., PET-Cu(Zn)-3(30), Fig. 5, S7 and S8). The more PET impurities presented, the more struvite crystals were formed, with up to 83.3 wt% and 97.8 wt% of struvite found in PET-Cu-30 and PET-Zn-30, respectively (Fig. 5b, S7b). These struvite crystals were embedded in PET surfaces (Fig. 5d-e) or coated over these impurities (Fig. S8b-c). In comparison to PE impurities, PET particulates are more likely to induce the formation of struvite under the same conditions, which may contribute to their much more oxygen-containing functional groups relative to PE particulates [46].

3.4. *Effect of HA on the precipitates reclaimed from BRs*

In contrast to the above MP impurities, the presence of HA impurities cannot fully suppress the formation of halite crystals even if its content is as high as 100 ppm (Figs. S9 and S10). However, as observed in the presence of low doses of PE impurities (viz. PE-Cu(Zn)-3), the introduction of HA significantly promotes the formation of newberyite (Fig. S9). Specifically, the more HA was added in the reactant mixtures, the more newberyite crystals were yielded, with a mass ratio as high as 95.4 wt% in the precipitate HA-100, 5.7 times the ratio in the blank sample (Fig. S9b). This might be attributed to the massive deprotonated carboxylic groups within HA molecules especially in alkaline solutions, which often show greater affinity towards ammonium than magnesium ions [64], thereby facilitating the formation of newberyite rather than struvite.

Interestingly, when 100 ppm of HA and 30 ppm of PET-Cu were added simultaneously in the reactant mixtures, the resulting precipitate (i.e., HA+PET-Cu) is featured by a small amount of rod-like newberyite and a large amount of needle-like struvite crystals (Fig. S10). WPF

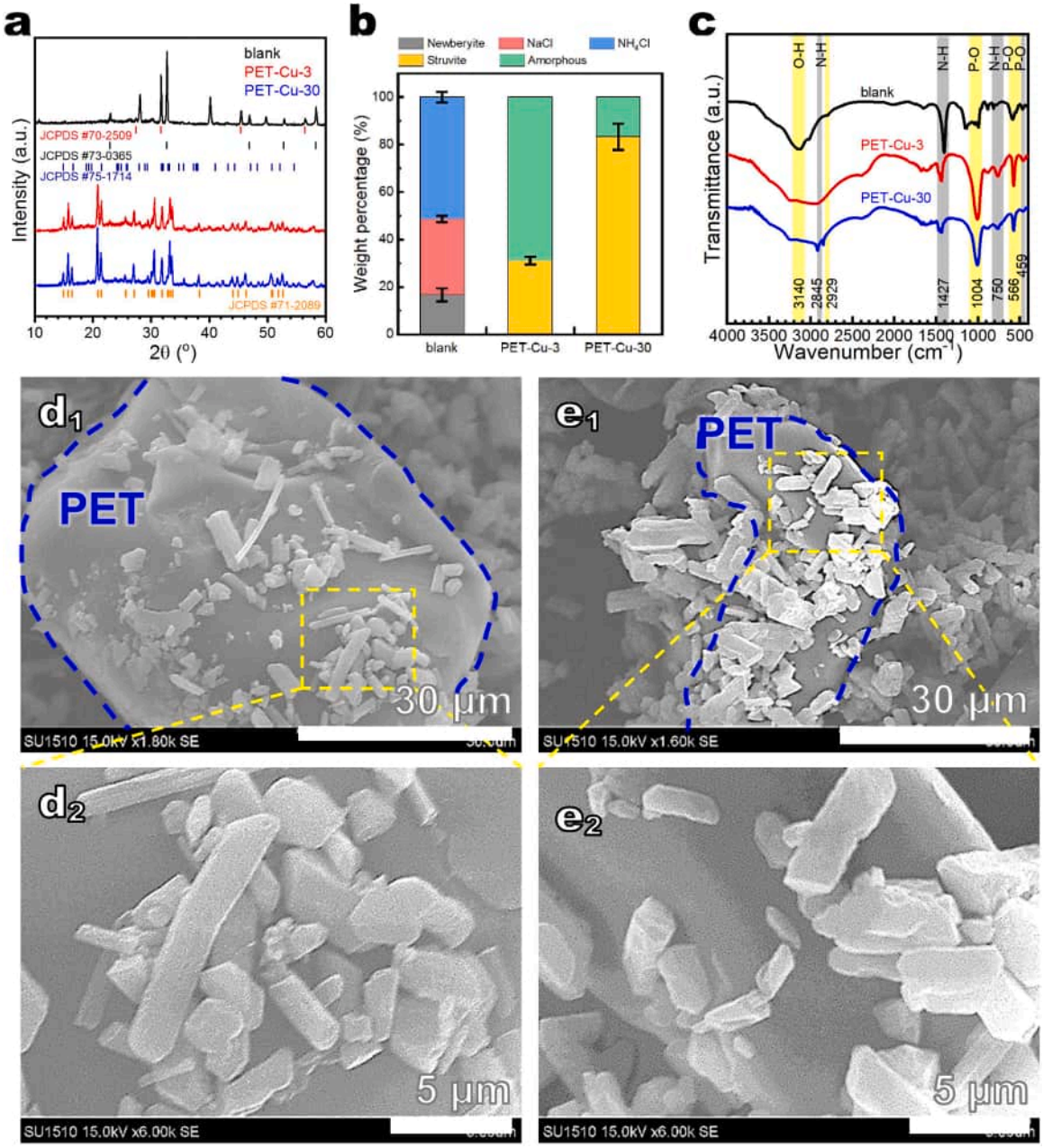

Fig. 5. Characterizations of precipitates from batch reactors with varying contents of PET-Cu. (**a**) XRD patterns (newberyite, JCPDS #75–1714; halite, JCPDS #70–2509; sal-ammoniac, JCPDS #73–0365; struvite, JCPDS #71–2089), (**b**) phase compositions, (**c**) FTIR spectra; SEM images of (**d**) the reclaimed precipitate with 3 mg L^{-1} PET-Cu, and (**e**) 30 mg L^{-1} PET-Cu.

refinement results indicate that it has a phase composition of 18.5 wt% newberyite and 81.5 wt% struvite (Fig. S9). These results are identical to the aforementioned observations that demonstrate the preference of PET impurities in inducing the formation of struvite (Fig. 5b, S7b), implying the potential seeding effect of such impurities during the struvite crystallization in BRs.

3.5. Effect of MPs and HA on the precipitates reclaimed from FBRs

As shown in Fig. 6, no newberyite crystals were found in all precipitates reclaimed from FBRs. A possible explanation would be that newberyite is less thermodynamically stable than farringtonite ($Mg_3(PO_4)_2$, JCPDS #88–0413) in solutions at 25 °C and 1 bar [65], which may lead to phase transformations from newberyite to farringtonite and struvite during the 6-day operation in FBRs. Different from the phase composition of the blank in BRs (Fig. 4b), the blank precipitate in FBRs is composed of 16.7 wt% struvite, 71.2 wt% farringtonite, and 12.1 wt% of amorphous phase (Fig. 6a-b). When 1 g L^{-1} of pure $MgNH_4PO_4{\cdot}6H_2O$ was introduced as seeds in the feed solutions, the amorphous component disappeared and the amount of struvite was increased to 31.7 wt% in the resulting precipitate denoted as seed (Fig. 6b). This phenomenon is as expected and indicates that seeds could enhance the transformation of amorphous components to struvite but not to farringtonite. Noticeably, the copresence of seed (1 g L^{-1}) and PET-Cu (30 ppm) impurities in the feed solution can further spur the formation of struvite, with 35.4 wt% of struvite found in the corresponding precipitate seed+PET-Cu (Fig. 6b). This observation verifies the seeding effect of PET particulates in FBR once again, as noted above in BRs (Fig. 5b).

In the case of using actual wastewater as the feed solution, its

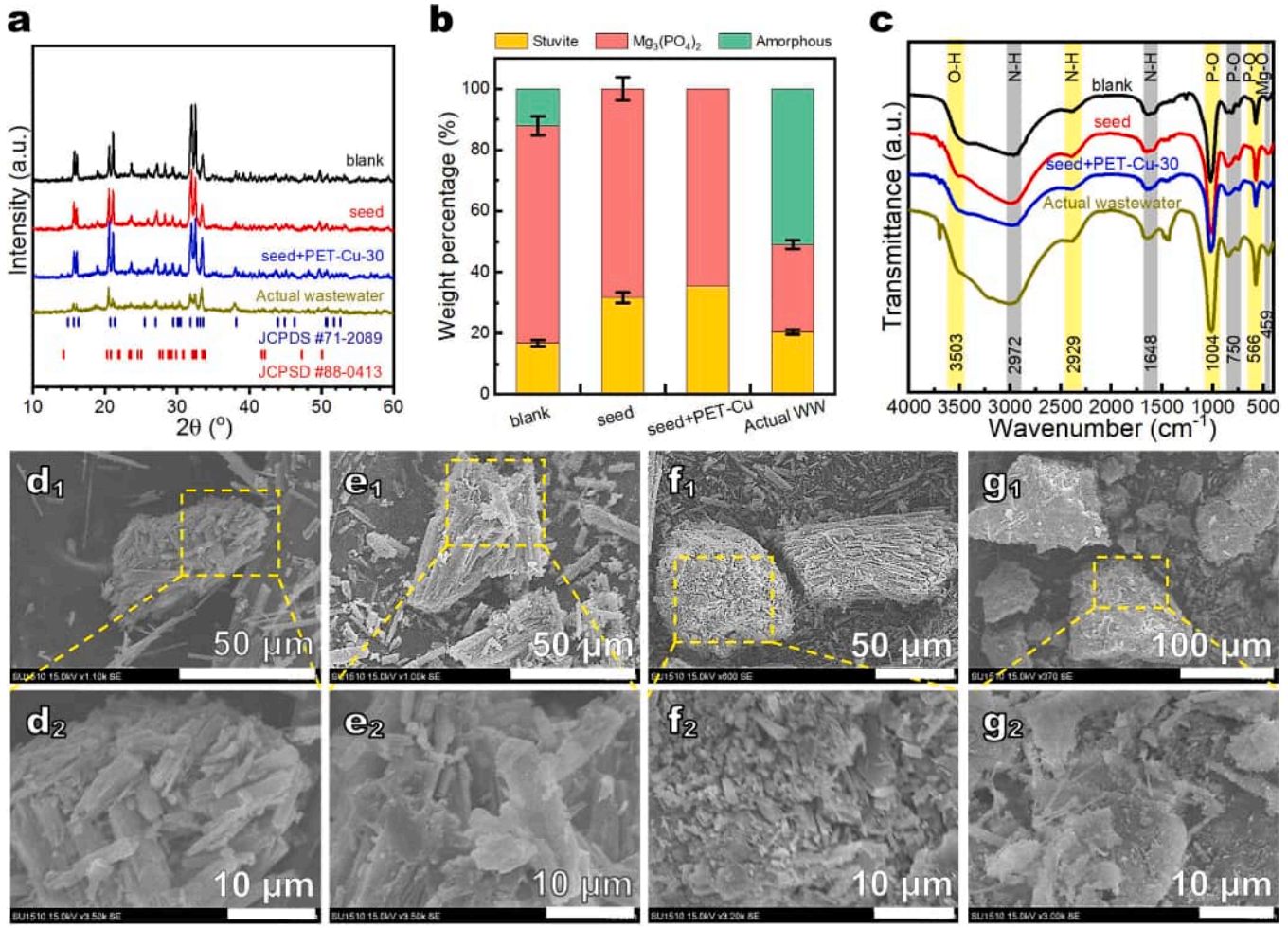

Fig. 6. Characterizations of precipitates in FBRs in the absence or presence of PE-Cu impurities. (**a**) XRD patterns (struvite, JCPDS #71–2089; trimagnesium bisphosphate-III (Mg3(PO4)2), JCPDS #88–0413), (**b**) phase compositions, (**c**) FTIR spectra; SEM images of (**d**) the control sample (i.e., sample from the blank suspension), (**e**) sample with 1 g L^{-1} seed, (**f**) 1 g L^{-1} seed + 30 mg L^{-1} PET-Cu, and (**g**) sample using the actual wastewater (sludge dewatering liquid) as influents.

phosphate concentration has been pre-adjusted up to 474 ppm, three times the P concentration in other feed solutions in FBRs. A preliminary experiment indicated that no precipitates were gained when using actual wastewater as the feed solution containing 158 ppm of P. It can be speculated that, based on the high COD concentration in the actual wastewater (Table S1), it is likely due to the high content of DOM in the feed solution which somewhat inhibited the formation of struvite [32, 35]. A large increase in the P concentration of the feed solution can effectively compensate for the inhibitory effect of DOM on struvite formation, yielding a precipitate with a phase composition of 20.4 wt% struvite (versus 16.7 wt% struvite in the blank), 28.6 wt% farringtonite, and 51 wt% amorphous components (Fig. 6b). The corresponding FTIR spectra with a group of typical infrared bands also confirmed the phase evolutions of these precipitates (Fig. 6c). SEM images indicate that all the precipitates in FBRs are featured by many irregular and compact agglomerates composed of numerous rod-like crystals (Fig. 6d-g). Note that the more the seed and/or PET impurities presented, the more compact the resulting precipitates were (Fig. 6f), in good agreement with earlier reports [1,24].

3.6. Roles of MPs and HA on struvite crystallization

The crystallization process can generally proceed in either heterogeneous or homogenous manners according to the classical nucleation theory [66]. Providing similar precursor elements and the same conditions, heterogeneous nucleation occurs more preferentially than homogenous nucleation as the free energy barrier for nucleation may be significantly reduced in the presence of colloidal or solid impurities [67]. Based on the above kinetic and characterization results, it is clear that MP and HA exerted quite different impacts on the crystallization reactions irrespective of the type of reactors where the reactions took place. Note that the MP impurities used are indiscerptible PE and PET particulates of ~ 50 μm in diameter (Figs. 4e, 5d). Therefore, the presence of either PE or PET renders the reaction system a heterogeneous one due to their large surfaces that are favorable for nucleation. The less in diameter and the rougher in surface, the more the free energy barrier of nucleation of phosphate crystals (e.g., struvite, newberyite, and farringtonite) would be reduced as the MP surface can stabilize the newly formed nuclei. Specifically, there are many defective domains as well as oxygen functional groups over the surface of aged PE and PET particulates [46], both of which are believed the most active binding centers for crystal-forming ions and/or monomers, thereby facilitating the following nucleation and crystallization of phosphate crystals [68]. Indeed, the presence of either PE or PET has induced faster nucleation and crystallization rates (Table 1), and a greater proportion of struvite in the reclaimed precipitates (Fig. 7a), verifying the seeding role of such impurities in struvite crystallization in BRs and/or FBRs [69,70].

Compared to aged PE, PET has a more polar and hydrophilic nature, e.g., much more abundance in carbonyl groups in aged PET than PET [46], and thereof more likely to capture NH_4^+ ions than aged PE. This in turn enlarges the Mg:N ratio of the synthetic suspensions, thus inducing the formation of struvite rather than newberyite [12,26]. This can well

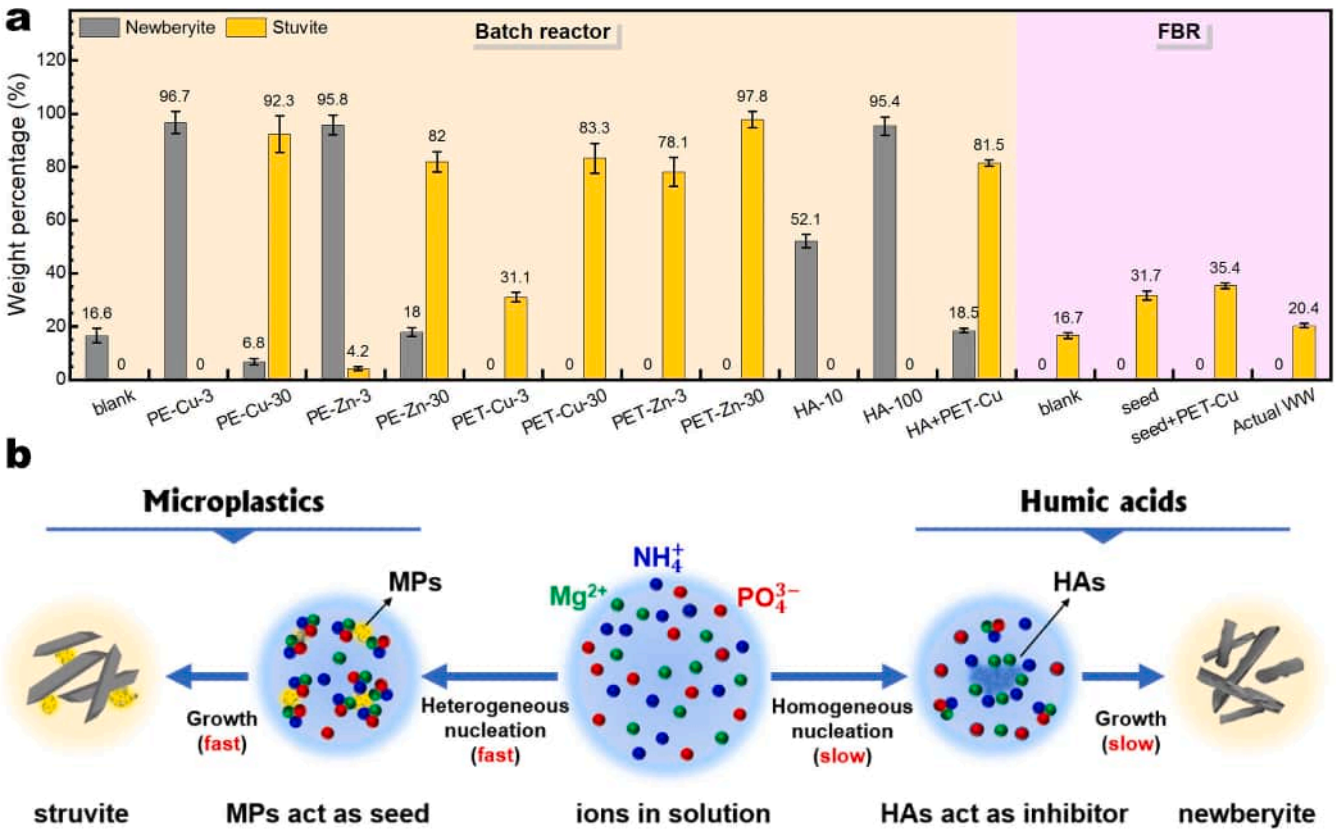

Fig. 7. (**a**) Weight percentage of newberyite and struvite in precipitates reclaimed from BRs and FBRs as a function of co-occurring impurities, (**b**) Schematical illustration of the roles of MPs and HA in struvite formation in BRs and FBRs.

explain why no newberyite was formed in the synthetic suspensions with only PET as the impurities (Fig. 7a) and clarify the observed higher struvite weight percentage with PET-Zn-3 (78.1 wt%) compared to PE-Zn-3 (4.2 wt%). Moreover, note that the presence of PE or PET impurities would introduce a trace amount of Cu^{2+} and Zn^{2+} ions into the synthetic suspensions, which can potentially influence struvite precipitation via many ways, such as co-precipitation with struvite [47], being adsorbed by struvite [48] and precipitation over the surface of struvite [49]. Since the amount of Cu^{2+} and Zn^{2+} introduced is trace and almost negligible (e.g., 87 μg Cu^{2+} L^{-1} or 105 μg Zn^{2+} L^{-1} would be introduced in the system with 30 mg L^{-1} of PE or PET and 157 mg L^{-1} of PO_4^{3-}), it's expected to have little impact on P removal. Interestingly, our data indicates that traces of Zn^{2+} ions are more likely than Cu^{2+} to induce the formation of struvite rather than newberyite, especially with a lower concentration of PE or PET as the impurities. A possible explanation is that Zn^{2+} has a higher ionic radius (~0.74 Å) and a more flexible coordination geometry, which enables it to form more stable complexes with the phosphate and ammonia species (NH_4^+) involved in struvite precipitation [71,72]. In contrast, Cu^{2+} ions have a smaller ionic radius (~0.73 Å) and a more rigid coordination geometry, which may limit their ability to facilitate struvite formation. This may account for the significant difference in struvite weight percentage between PET-Zn-3 (78.1 wt%) and PET-Cu-3 (31.1 wt%). Nevertheless, it's essential to note that the preference for phase formation may also depend on kinetic factors, which may need further exploration in subsequent studies.

On the contrary, HA is a group of soluble macromolecules rich in carboxyl and carbonyl groups, which are likely to bind struvite-forming cations, and nuclei in aqueous solutions [60]. This interaction appears to reduce the solution supersaturation and increase the energy barrier of nucleation, prolonging the induction time of nucleation and subsequent crystallization (Table 1) [32,62]. Besides, as discussed above, the presence of HA appears to create a favorable environment for newberyite formation (Fig. 7a), yielding a much higher proportion of rod-shaped newberyite crystals in the presence of 100 ppm HA as impurities (Figs. S9 and S10). This observation is in good agreement with previous reports [32,33]. In light of the above results, the roles of MPs and HA in struvite formation have been rationally proposed and illustrated schematically in Fig. 7b. Specifically, MPs can lower the free energy barrier of struvite formation by providing quite large defective surfaces that serve as nucleation sites even though both MP surface and struvite nuclei are negatively charged (Fig. S11). However, HA plays an inhibitory role in mediating the formation of struvite, probably through a complex of interactions including bridge complexation, static Coulomb interaction, and so on. Collectively, both PE and PET particulates serve as seeding materials spurring nucleation and subsequent crystallization of struvite crystals in BRs and/or FBRs, while HA seems to inhibit the formation of struvite but facilitate newberyite formation due to complex interactions [73]. To this end, more investigations are needed to elucidate the mechanism for this extraordinary role of HA impurities on the molecular level.

4. Conclusions

This study has comprehensively elucidated the roles of aged MP and HA impurities in the struvite crystallization process in batch and fluidized-bed reactors. The crystallization kinetic results reveal that the presence of aged MPs significantly increases the nucleation and growth rate of such crystals, primarily because the large surfaces of MPs can serve as reactive sites for newly formed nuclei, reducing the free energy barrier of nucleation and thereby expediting the growth of struvite in solutions. HA, on the other hand, inhibits the nucleation and growth of struvite crystals but favors the formation of newberyite crystals. Interestingly, the co-presence of MPs and HA can significantly compensate for the inhibitory effects of humic acid on the formation rate of struvite,

yielding a precipitate dominated by struvite. Moreover, it also showed that the presence of MPs and/or HA can significantly impact the quality of the resulting precipitates from struvite crystallization, leading to complex changes in both the phase compositions and the morphology. From an environmental perspective, these findings provide crucial insights into a previously underexplored interaction between MPs, humic substances, and crystal-forming ions during P recovery processes in BRs and FBRs. However, the effects of other factors such as pH and Mg:N:P ratio on struvite formation in the presence of the above impurities may deserve further exploration. To understand the molecular-scale interactions of these species at the MP/water interface, future studies are required by using *in situ* spectroscopic tools (e.g., *in situ* X-ray absorption (XAS) spectroscopy), and therefore unveiling the molecular roles of both impurities in struvite nucleation and growth. Given the ubiquity of microplastics and humic substances in wastewater, our study underscores the importance of considering the impact of microplastics on nutrient recovery technologies and highlights the necessity of tailored approaches to mitigate their adverse effects on the efficiency of recovering nutrients in the form of struvite and the quality of the reclaimed struvite, with significant implications for wastewater treatment and sustainable agriculture.

CRediT authorship contribution statement

Feihu Li: Writing – review & editing, Writing – original draft, Supervision, Project administration, Investigation, Funding acquisition, Conceptualization. **Junna Yan:** Visualization, Methodology, Investigation. **Mengyu Ma:** Methodology, Investigation.

Declaration of Competing Interest

The authors declare that they have no known competing financial interests or personal relationships that could have appeared to influence the work reported in this paper.

Data availability

Data will be made available on request.

Acknowledgments

This work is financially supported by the National Natural Science Foundation of China (NSFC, No. 51002080). The authors are grateful to Nanjing Qiaobei Sewage Treatment Plant for providing the actual wastewater sample, and to Dr. Fengying Li for her assistance in XRF analysis.

Appendix A. Supporting information

Supplementary data associated with this article can be found in the online version at doi:10.1016/j.jhazmat.2024.135108.

References

[1] Desmidt, E., Ghyselbrecht, K., Zhang, Y., Pinoy, L., Van der Bruggen, B., Verstraete, W., Rabaey, K., Meesschaert, B., 2015. Global phosphorus scarcity and full-scale p-recovery techniques: a review. Crit Rev Environ Sci Technol 45, 336–384. https://doi.org/10.1080/10643389.2013.866531.

[2] Alewell, C., Ringeval, B., Ballabio, C., Robinson, D.A., Panagos, P., Borrelli, P., 2020. Global phosphorus shortage will be aggravated by soil erosion. Nat Commun 11, 4546. https://doi.org/10.1038/s41467-020-18326-7.

[3] Cordell, D., Drangert, J.O., White, S., 2009. The story of phosphorus: global food security and food for thought. Glob Environ Change-Hum Policy Dimens 19, 292–305. https://doi.org/10.1016/j.gloenvcha.2008.10.009.

[4] Vaccari, D.A., Powers, S.M., Liu, X., 2019. Demand-driven model for global phosphate rock suggests paths for phosphorus sustainability. Environ Sci Technol 53, 10417–10425. https://doi.org/10.1021/acs.est.9b02464.

[5] Withers, P.J.A., Elser, J.J., Hilton, J., Ohtake, H., Schipper, W.J., van Dijkf, K.C., 2015. Greening the global phosphorus cycle: how green chemistry can help achieve planetary P sustainability. Green Chem 17, 2087–2099. https://doi.org/10.1039/c4gc02445a.

[6] Rockstrom, J., Steffen, W., Noone, K., Persson, A., Chapin, F.S., Lambin, E.F., Lenton, T.M., Scheffer, M., Folke, C., Schellnhuber, H.J., Nykvist, B., de Wit, C.A., Hughes, T., van der Leeuw, S., Rodhe, H., Sorlin, S., Snyder, P.K., Costanza, R., Svedin, U., Falkenmark, M., Karlberg, L., Corell, R.W., Fabry, V.J., Hansen, J., Walker, B., Liverman, D., Richardson, K., Crutzen, P., Foley, J.A., 2009. A safe operating space for humanity. Nature 461, 472–475. https://doi.org/10.1038/461472a.

[7] Jupp, A.R., Beijer, S., Narain, G.C., Schipper, W., Slootweg, J.C., 2021. Phosphorus recovery and recycling - closing the loop. Chem Soc Rev 50, 87–101. https://doi.org/10.1039/d0cs01150a.

[8] Yeoman, S., Stephenson, T., Lester, J.N., Perry, R., 1988. The removal of phosphorus during wastewater treatment - a review. Environ Pollut 49, 183–233. https://doi.org/10.1016/0269-7491(88)90209-6.

[9] Morse, G.K., Brett, S.W., Guy, J.A., Lester, J.N., 1998. Review: Phosphorus removal and recovery technologies. Sci Total Environ 212, 69–81. https://doi.org/10.1016/S0048-9697(97)00332-X.

[10] de-Bashan, L.E., Bashan, Y., 2004. Recent advances in removing phosphorus from wastewater and its future use as fertilizer (1997-2003). Water Res 38, 4222–4246. https://doi.org/10.1016/j.watres.2004.07.014.

[11] Mehta, C.M., Khunjar, W.O., Nguyen, V., Tait, S., Batstone, D.J., 2015. Technologies to recover nutrients from waste streams: a critical review. Crit Rev Environ Sci Technol 45, 385–427. https://doi.org/10.1080/10643389.2013.866621.

[12] Le Corre, K.S., Valsami-Jones, E., Hobbs, P., Parsons, S.A., 2009. Phosphorus recovery from wastewater by struvite crystallization: a review. Crit Rev Environ Sci Technol 39, 433–477. https://doi.org/10.1080/10643380701640573.

[13] Wang, H., Wang, X.J., Li, J., Jing, H.P., Xia, S.Q., Liu, F.Q., Zhao, J.F., 2018. Comparison of palygorskite and struvite supported palygorskite derived from phosphate recovery in wastewater for in-situ immobilization of Cu, Pb and Cd in contaminated soil. J Hazard Mater 346, 273–284. https://doi.org/10.1016/j.jhazmat.2017.12.042.

[14] Borgerding, J., 1972. Phosphate deposits in digestion systems. J Water Pollut Control Fed 44, 813–829. https://doi.org/10.2307/25037456.

[15] Doyle, J.D., Parsons, S.A., 2002. Struvite formation, control and recovery. Water Res 36, 3925–3940. https://doi.org/10.1016/S0043-1354(02)00126-4.

[16] Battistoni, P., Pavan, P., Cecchi, F., Mata-Alvarez, J., 1998. Phosphate removal in real anaerobic supernatants: Modelling and performance of a fluidized bed reactor. Water Sci Technol 38, 275–283. https://doi.org/10.1016/S0273-1223(98)00412-0.

[17] Woods, N.C., Sock, S.M., Daigger, G.T., 1999. Phosphorus recovery technology modeling and feasibility evaluation for municipal wastewater treatment plants. Environ Technol 20, 663–679. https://doi.org/10.1080/09593332008616862.

[18] Zin, M.M.T., Kim, D.J., 2021. Simultaneous recovery of phosphorus and nitrogen from sewage sludge ash and food wastewater as struvite by Mg-biochar. J Hazard Mater 403, 123704. https://doi.org/10.1016/j.jhazmat.2020.123704.

[19] Chen, X.J., Jin, Y.C., Zhou, Z.J., Huang, P.W., Chen, X., Ding, R., Chen, R.Y., 2022. Spontaneous nutrient recovery and disinfection of aquaculture wastewater via Mg-coconut shell carbon composites. J Hazard Mater 426, 128119. https://doi.org/10.1016/j.jhazmat.2021.128119.

[20] Ohlinger, K.N., Young, T.M., Schroeder, E.D., 2000. Postdigestion struvite precipitation using a fluidized bed reactor. J Environ Eng-Asce 126, 361–368. https://doi.org/10.1061/(Asce)0733-9372(2000)126:4(361).

[21] Battistoni, P., De Angelis, A., Pavan, P., Prisciandaro, M., Cecchi, F., 2001. Phosphorus removal from a real anaerobic supernatant by struvite crystallization. Water Res 35, 2167–2178. https://doi.org/10.1016/S0043-1354(00)00498-X.

[22] Ueno, Y., Fujii, M., 2001. Three years experience of operating and selling recovered struvite from full-scale plant. Environ Technol 22, 1373–1381. https://doi.org/10.1080/09593332208618196.

[23] Britton, A., Koch, F.A., Mavinic, D.S., Adnan, A., Oldham, W.K., Udala, B., 2005. Pilot-scale struvite recovery from anaerobic digester supernatant at an enhanced biological phosphorus removal wastewater treatment plant. J Environ Eng Sci 4, 265–277. https://doi.org/10.1139/S04-059.

[24] Forrest, A.L., Fattah, K.P., Mavinic, D.S., Koch, F.A., 2008. Optimizing struvite production for phosphate recovery in WWTP. J Environ Eng-Asce 134, 395–402. https://doi.org/10.1061/(Asce)0733-9372(2008)134:5(395).

[25] Jaffer, Y., Clark, T.A., Pearce, P., Parsons, S.A., 2002. Potential phosphorus recovery by struvite formation. Water Res 36, 1834–1842. https://doi.org/10.1016/S0043-1354(01)00391-8.

[26] Shih, Y.J., Abarca, R.R.M., de Luna, M.D.G., Huang, Y.H., Lu, M.C., 2017. Recovery of phosphorus from synthetic wastewaters by struvite crystallization in a fluidized-bed reactor: Effects of pH, phosphate concentration and coexisting ions. Chemosphere 173, 466–473. https://doi.org/10.1016/j.chemosphere.2017.01.088.

[27] Guan, Q., Zeng, G.S., Gong, B.C.A., Li, Y.P., Ji, H.Y., Zhang, J.F., Song, J.T., Liu, C. L., Wang, Z.B., Deng, C.J., 2021. Phosphorus recovery and iron, copper precipitation from swine wastewater via struvite crystallization using various magnesium compounds. J Clean Prod 328, 129588. https://doi.org/10.1016/j.jclepro.2021.129588.

[28] Zhang, T., Wu, X.S., Shaheen, S.M., Abdelrahman, H., Ali, E.F., Bolan, N.S., Ok, Y. S., Li, G.X., Tsang, D.C.W., Rinklebe, J., 2022. Improving the humification and phosphorus flow during swine manure composting: A trial for enhancing the beneficial applications of hazardous biowastes. J Hazard Mater 425, 127906. https://doi.org/10.1016/j.jhazmat.2021.127906.

[29] Bouropoulos, N.C., Koutsoukos, P.G., 2000. Spontaneous precipitation of struvite from aqueous solutions. J Cryst Growth 213, 381–388. https://doi.org/10.1016/S0022-0248(00)00351-1.
[30] Matynia, A., Koralewska, J., Wierzbowska, B., Piotrowski, K., 2006. The influence of process parameters on struvite continuous crystallization kinetics. Chem Eng Commun 193, 160–176. https://doi.org/10.1080/009864490949008.
[31] Bah, A.T., Shen, Z.Y., Yan, J.N., Li, F.H., 2023. Phosphorous recovery from water via batch adsorption enrichment combined with struvite crystallization in a fluidized bed reactor. J Environ Chem Eng 11, 110180. https://doi.org/10.1016/j.jece.2023.110180.
[32] Zhang, Q., Zhao, S.P., Ye, X.Z., Xiao, W.D., 2016. Effects of organic substances on struvite crystallization and recovery. Desalin Water Treat 57, 10924–10933. https://doi.org/10.1080/19443994.2015.1040850.
[33] Wang, W.M., Xin, X., Li, B., Huang, H.M., Liu, X.N., Song, L., Wu, X.F., Huang, Y.F., 2022. Effect of organics on Cu and Cr in recovered struvite from synthetic swine wastewater. J Clean Prod 360, 132186. https://doi.org/10.1016/j.jclepro.2022.132186.
[34] Ge, K., Ji, Y.H., Tang, S., 2020. Crystallization kinetics and mechanism of magnesium ammonium phosphate hexahydrate: experimental investigation and chemical potential gradient model analysis and prediction. Ind Eng Chem Res 59, 13799–13809. https://doi.org/10.1021/acs.iecr.0c01840.
[35] Rabinovich, A., Rouff, A.A., 2021. Effect of phenolic organics on the precipitation of struvite from simulated dairy wastewater. ACS EST Water 1, 910–918. https://doi.org/10.1021/acsestwater.0c00234.
[36] Kofina, A.N., Demadis, K.D., Koutsoukos, P.G., 2007. The effect of citrate and phosphocitrate on struvite spontaneous precipitation. Cryst Growth Des 7, 2705–2712. https://doi.org/10.1021/cg0603927.
[37] Wang, Y., Wang, X.J., Li, Y., Liu, Y.Y., Sun, Y., Xia, S.Q., Zhao, J.F., 2021. Effects of coexistence of tetracycline, copper and microplastics on the fate of antibiotic resistance genes in manured soil. Sci Total Environ 790, 148087. https://doi.org/10.1016/j.scitotenv.2021.148087.
[38] Hu, T.Y., He, P.J., Yang, Z., Wang, W., Zhang, H., Shao, L.M., Lu, F., 2022. Emission of airborne microplastics from municipal solid waste transfer stations in downtown. Sci Total Environ 828, 154400. https://doi.org/10.1016/j.scitotenv.2022.154400.
[39] Gao, D.G., Li, B., Huang, X.W., Liu, X.N., Li, R.L., Ye, Z.L., Wu, X.F., Huang, Y.F., Wang, G.Q., 2023. A review of the migration mechanism of antibiotics during struvite recovery from wastewater. Chem Eng J 466, 142983. https://doi.org/10.1016/j.cej.2023.142983.
[40] Woldeyohannis, N.N., Desta, A.F., 2023. Fate of antimicrobial resistance genes (ARG) and ARG carriers in struvite production process from human urine. J Environ Sci Health Part A Toxic/Hazard Subst Environ Eng 58, 783–792. https://doi.org/10.1080/10934529.2023.2235246.
[41] Wu, R.T., Cai, Y.F., Chen, Y.X., Yang, Y.W., Xing, S.C., Liao, X.D., 2021. Occurrence of microplastic in livestock and poultry manure in South China. Environ Pollut 277, 116790. https://doi.org/10.1016/j.envpol.2021.116790.
[42] Zhang, S.W., Li, Y.X., Chen, X.C., Jiang, X.M., Li, J., Yang, L., Yin, X.Q., Zhang, X.L., 2022. Occurrence and distribution of microplastics in organic fertilizers in China. Sci Total Environ 844, 157061. https://doi.org/10.1016/j.scitotenv.2022.157061.
[43] Koelmans, A.A., Bakir, A., Burton, G.A., Janssen, C.R., 2016. Microplastic as a vector for chemicals in the aquatic environment: critical review and model-supported reinterpretation of empirical studies. Environ Sci Technol 50, 3315–3326. https://doi.org/10.1021/acs.est.5b06069.
[44] Mlinaric, N.M., Selmani, A., Brkic, A.L., Dzakula, B.N., Kralj, D., Kontrec, J., 2022. Exposure of microplastics to organic matter in waters enhances microplastic encapsulation into calcium carbonate. Environ Chem Lett 20, 2235–2242. https://doi.org/10.1007/s10311-022-01433-w.
[45] Wang, Q.J., Zhang, Y., Wangjin, X.X., Wang, Y.L., Meng, G.H., Chen, Y.H., 2020. The adsorption behavior of metals in aqueous solution by microplastics effected by UV radiation. J Environ Sci - China 87, 272–280. https://doi.org/10.1016/j.jes.2019.07.006.
[46] Ma, M.Y., Li, F.H., 2023. Insights into the adsorption of copper/zinc ions over aged polyethylene and polyethylene terephthalate microplastics. ChemRxiv https://doi.org/10.26434/chemrxiv-2023-q52xg.
[47] Muryanto, S., Bayuseno, A.P., 2014. Influence of Cu^{2+} and Zn^{2+} as additives on crystallization kinetics and morphology of struvite. Powder Technol 253, 602–607. https://doi.org/10.1016/j.powtec.2013.12.027.
[48] Perwitasari, D.S., Muryanto, S., Jamari, J., Bayuseno, A.P., 2018. Kinetics and morphology analysis of struvite precipitated from aqueous solution under the influence of heavy metals: Cu^{2+}, Pb^{2+}, Zn^{2+}. J Environ Chem Eng 6, 37–43. https://doi.org/10.1016/j.jece.2017.11.052.
[49] Tang, C.J., Liu, Z.G., Peng, C., Chai, L.Y., Kuroda, K., Okido, M., Song, Y.X., 2019. New insights into the interaction between heavy metals and struvite: Struvite as platform for heterogeneous nucleation of heavy metal hydroxide. Chem Eng J 365, 60–69. https://doi.org/10.1016/j.cej.2019.02.034.
[50] Li, F.H., Wu, W.H., Li, R.Y., Fu, X.R., 2016. Adsorption of phosphate by acid-modified fly ash and palygorskite in aqueous solution: Experimental and modeling. Appl Clay Sci 132, 343–352. https://doi.org/10.1016/j.clay.2016.06.028.
[51] Nelson, N.O., Mikkelsen, R.L., Hesterberg, D.L., 2003. Struvite precipitation in anaerobic swine lagoon liquid: effect of pH and Mg: P ratio and determination of rate constant. Bioresour Technol 89, 229–236. https://doi.org/10.1016/S0960-8524(03)00076-2.
[52] Wang, F., Wang, B., Duan, L., Zhang, Y.Z., Zhou, Y.T., Sui, Q., Xu, D.J., Qu, H., Yu, G., 2020. Occurrence and distribution of microplastics in domestic, industrial, agricultural and aquacultural wastewater sources: a case study in Changzhou, China. Water Res 182, 115956. https://doi.org/10.1016/j.watres.2020.115956.
[53] Ridzuan Anoam, S., Abdul Hakim Lim, M.F., Abdul Halim, M.H., Abdul Manan, S., Mohd Ali, M., Jansar, K.M., 2022. Microplastic abundance from pig farm effluent and surface water in Sungai Tuang, Melaka, Malaysia. Malays Appl Biol 51, 85–95. https://doi.org/10.55230/mabjournal.v51i5.2359.
[54] Yan, J.N., Ma, M.Y., Zhao, B., Li, F.H., 2023. Phosphate recovery from wastewater by rapid adsorption-desorption enrichment over UiO-66@melamine sponge composites. J Water Process Eng 55, 104253. https://doi.org/10.1016/j.jwpe.2023.104253.
[55] Zhou, Y.X., Li, Y.P., Yan, Z.H., Wang, H.Y., Chen, H.J., Zhao, S.S., Zhong, N.Q., Cheng, Y., Acharya, K., 2023. Microplastics discharged from urban drainage system: Prominent contribution of sewer overflow pollution. Water Res 236, 119976. https://doi.org/10.1016/j.watres.2023.119976.
[56] Ye, Z.L., Deng, Y.J., Lou, Y.Y., Ye, X., Zhang, J.Q., Chen, S.H., 2017. Adsorption behavior of tetracyclines by struvite particles in the process of phosphorus recovery from synthetic swine wastewater. Chem Eng J 313, 1633–1638. https://doi.org/10.1016/j.cej.2016.11.062.
[57] Bhuiyan, M.I.H., Mavinic, D.S., Beckie, R.D., 2008. Nucleation and growth kinetics of struvite in a fluidized bed reactor. J Cryst Growth 310, 1187–1194. https://doi.org/10.1016/j.jcrysgro.2007.12.054.
[58] Agrawal, S., Guest, J.S., Cusick, R.D., 2018. Elucidating the impacts of initial supersaturation and seed crystal loading on struvite precipitation kinetics, fines production, and crystal growth. Water Res 132, 252–259. https://doi.org/10.1016/j.watres.2018.01.002.
[59] Ge, X.F., Wang, L.J., Zhang, W.J., Putnis, C.V., 2020. Molecular understanding of humic acid-limited phosphate precipitation and transformation. Environ Sci Technol 54, 207–215. https://doi.org/10.1021/acs.est.9b05145.
[60] Gerke, J., 2021. The effect of humic substances on phosphate and iron acquisition by higher plants: qualitative and quantitative aspects. J Plant Nutr Soil Sci 184, 329–338. https://doi.org/10.1002/jpln.202000525.
[61] Avena, M.J., Koopal, L.K., van Riemsdijk, W.H., 1999. Proton binding to humic acids: electrostatic and intrinsic interactions. J Colloid Interface Sci 217, 37–48. https://doi.org/10.1006/jcis.1999.6317.
[62] Song, Y.H., Dai, Y.R., Hu, Q., Yu, X.H., Qian, F., 2014. Effects of three kinds of organic acids on phosphorus recovery by magnesium ammonium phosphate (MAP) crystallization from synthetic swine wastewater. Chemosphere 101, 41–48. https://doi.org/10.1016/j.chemosphere.2013.11.019.
[63] Tansel, B., Lunn, G., Monje, O., 2018. Struvite formation and decomposition characteristics for ammonia and phosphorus recovery: A review of magnesium-ammonia-phosphate interactions. Chemosphere 194, 504–514. https://doi.org/10.1016/j.chemosphere.2017.12.004.
[64] Schwierz, N., Horinek, D., Netz, R.R., 2015. Specific ion binding to carboxylic surface groups and the ph dependence of the Hofmeister Series. Langmuir 31, 215–225. https://doi.org/10.1021/la503813d.
[65] Lothenbach, B., Xu, B.W., Winnefeld, F., 2019. Thermodynamic data for magnesium (potassium) phosphates. Appl Geochem 111, 104450. https://doi.org/10.1016/j.apgeochem.2019.104450.
[66] De Yoreo, J.J., Nakouzi, E., Jin, B., Chun, J., Mundy, C.J., 2022. Spiers memorial lecture: assembly-based pathways of crystallization. Faraday Discuss 235, 9–35. https://doi.org/10.1039/d2fd00061j.
[67] Wang, L.J., Nancollas, G.H., 2008. Calcium orthophosphates: crystallization and dissolution. Chem Rev 108, 4628–4669. https://doi.org/10.1021/cr0782574.
[68] Lei, Y., Zhan, Z.S., Saakes, M., van der Weijden, D.R., Buisman, J.N.C., 2021. Electrochemical recovery of phosphorus from wastewater using tubular stainless-steel cathode for a scalable long-term operation. Water Res 199, 117199. https://doi.org/10.1016/j.watres.2021.117199.
[69] Song, Y.H., Qiu, G.L., Yuan, P., Cui, X.Y., Peng, J.F., Zeng, P., Duan, L., Xiang, L.C., Qian, F., 2011. Nutrients removal and recovery from anaerobically digested swine wastewater by struvite crystallization without chemical additions. J Hazard Mater 190, 140–149. https://doi.org/10.1016/j.jhazmat.2011.03.015.
[70] Li, B., Huang, H.M., Boiarkina, I., Yu, W., Huang, Y.F., Wang, G.Q., Young, B.R., 2019. Phosphorus recovery through struvite crystallisation: Recent developments in the understanding of operational factors. J Environ Manag 248, 109254. https://doi.org/10.1016/j.jenvman.2019.07.025.
[71] Papadopoulos, P., Rowell, D.L., 1989. The reactions of copper and zinc with calcium carbonate surfaces. J Soil Sci 40, 39–48. https://doi.org/10.1111/j.1365-2389.1989.tb01252.x.
[72] Clark, B., Sharma, N., Apraku, E., Dong, H., Tarpeh, W.A., 2024. Ligand exchange adsorbents for selective phosphate and total ammonia nitrogen recovery from wastewaters. Acc Mater Res 5, 492–504. https://doi.org/10.1021/accountsmr.3c00290.
[73] Kim, D., Wu, T., Cohen, M., Jeon, I., Jun, Y.S., 2018. Designing the crystalline structure of calcium phosphate seed minerals in organic templates for sustainable phosphorus management. Green Chem 20, 534–543. https://doi.org/10.1039/c7gc02634j.